A Glider Network Design Study for a Synoptic View of the Oceanic Mesoscale Variability

Blandine L'Hévéder, Laurent Mortier, Pierre Testor, François Lekien

A Glider Network Design Study for a Synoptic View of the Oceanic Mesoscale Variability

BLANDINE L'HÉVÉDER

Laboratoire de Météorologie Dynamique, Paris, France

LAURENT MORTIER

Ecole Nationale Supérieure de Techniques Avancées, Paris, France

PIERRE TESTOR

Laboratoire d'Océanographie et du Climat: Expérimentations et Approches Numériques, Paris, France

FRANÇOIS LEKIEN

Université Libre de Bruxelles, Brussels, Belgium

(Manuscript received 27 February 2012, in final form 31 January 2013)

ABSTRACT

This study presents an Observing System Simulation Experiment (OSSE) with a network of gliders in a realistic mesoscale field of eddies and filaments. The main objective is to demonstrate that the analysis skill evaluation, performed with different statistics, determines the optimal number of gliders needed to survey a ''glider observatory'' with a given simple topology of the glider array, in the shape of a ''double comb.'' Metrics, based on a spatial interpolation of the sampled data with a multiscale objective analysis method, are elaborated to evaluate the reconstruction of the three-dimensional temperature field with several glider networks, at a weekly time scale. The mesoscale structures obtained by the optimal network (front, eddies, eddies detachment) are also compared with the structures of the original simulation. This comparison demonstrates the efficiency of a glider fleet to sample a well-defined area at a given spatiotemporal scale. In this particular situation (midlatitude region, domain of 400 km $\times$ 600 km, reconstruction of weekly snapshots), the optimum network is composed of 10 gliders. A relationship is highlighted between the spatial scales of the sampled area, the physical characteristics of the studied region, the reconstruction time scale, and the optimum number of gliders. The results presented here can be applied to design an actual in situ experiment.

1. Introduction

Mesoscale and submesoscale features (horizontal scales from 10 to 100 km and time scales from a few days to months or even years) such as eddies, fronts, large-scale waves, filaments, and stirring regions are ubiquitous in the ocean, in particular at midlatitudes. They are associated with horizontal velocities up to 1–2 m s^{-1} as well as vertical velocities of 10–100 m day^{-1} (Griffiths and Hopfinger 1984. They are often linked to large-scale horizontal thermohaline gradients and ocean fronts in the form of frontal meanders and eddies, which can be generated by several types of 3D instability mechanisms involving the entire water column. They can be responsible for significant large-scale transport of mass, energy (Stammer 1998), and matter or dissolved substances. Indeed, secondary circulations at submesoscale (filaments, small eddies of spatial scales from 1 to 10 km), associated with strong stirring and vertical velocities, are superimposed on this mesoscale field (Lévy et al. 2012). In fact, the mesoscale field has to be taken into account to close the energy, mass, and matter budgets of any oceanic region because a lot of turbulent energy is trapped at this scale. This makes them a key element for governing the ocean general circulation with important consequences for climate but also for marine

Corresponding author address: Blandine L'Hévéder, LMD, UPMC, Boite 99, 4 Place Jussieu, Paris 75005, France.
E-mail: blh@locean-ipsl.upmc.fr

DOI: 10.1175/JTECH-D-12-00053.1

ecosystems, as they govern the biogeochemical cycles and the transport of marine living species (Mann and Lazier 2005).

Since the Midocean Dynamics Experiment (MODE) in the early 1970s (Olbers 1978), eddies and mesoscale features in general have received considerable attention with in situ experiments from the oceanographic community. With standard CTD casts, expendable probes, and even towed devices, research vessels can give a reasonable 3D view of such structures with a relatively high spatial resolution. However, they are very limited by time factors, making it difficult to capture a synoptic view and the temporal variability of the mesoscale processes. On the other hand, a mooring network can provide a high temporal resolution, but it is drastically limited by the small number of moorings that can be reasonably set up because of technical constraints and the minimum distance between two adjacent moorings.

During the same period, satellite altimetry has started to give very novel quasi-synoptic images of these mesoscale structures at the sea surface (Cheney and Marsh 1981). The considerable development of satellite altimetry has allowed the routine acquisition of detailed information of mesoscale movements with a reasonable space and time resolution, and the compilation of statistics of their surface signature (Stammer 1997). The next generation of altimetric missions will even permit us to reach a higher resolution, starting to cover the submesoscale range. However, as a fundamental limitation, altimetry does not provide any information about the subsurface and deep signature of mesoscale features.

A major change came during the last decades with a new class of small autonomous underwater vehicles (AUVs) envisioned by Henry Stommel 20 years before (Stommel 1989). Underwater gliders are autonomous vehicles equipped with a buoyancy engine allowing them to glide during long periods along a sawtooth trajectory and to carry out vertical yos from the surface to depths of about 1000 m, up to several months. They can be remotely steered, so the collection of data can be controlled with a high accuracy. They can be equipped with a wide variety of sensors: CTD (conductivity–temperature–depth), ADCP, fluorimeters for chlorophyll a (ChlA) and colored dissolved organic matter (CDOM), turbidity sensor, oxygen sensor, nitrate sensors, hydrophones, etc., which makes them very attractive to investigate the deep ecosystems and to push back the last frontier in the deep ocean. Along their trajectory, they sample the ocean interior with a high vertical resolution (a few meters) while the distance between two successive slanted profiles varies from some hundreds of meters up to a few kilometers, depending on the maximum depth. Their relatively low cost compared to a ship cruise and their long lifetime in operation make it feasible to deploy tens of gliders together during a few months. Unlike the profilers of the Argo network (Roemmich et al. 2009), which drift freely and split up, the remote steering capability of gliders allows them to fly in cooperative fleets and to concentrate measurements in the same area. It has been early envisioned that such networks of gliders should be adapted to sample the ocean interior at mesoscale resolution with a good degree of synoptic character (Rudnick et al. 2004), similar to what is achieved for the sea surface topography by satellite altimetry. Because of the characteristics of gliders available nowadays and the need for complementarity with other ocean observing networks, such as the Argo network, the concept of a ''glider observatory'' at a regional focus has been raised. Typically, a glider observatory is a box of up to 1000 km $\times$ 1000 km dimension that a glider can cross in a few weeks. It should be located in oceanic regions that are key for the oceans' monitoring, such as water formation areas, western boundary current regions, eastern boundary upwelling regions, or large bays where buoyant coastal currents can intrude (Testor et al. 2010).

These visions have motivated several types of studies and some pioneering experiments at sea, such as the first and second Autonomous Ocean Sampling Network (AOSN I and AOSN II, respectively) programs in the Monterey Bay Experiment and the Adaptive Sampling and Prediction (ASAP) program (Ramp et al. 2009), where a network of gliders was coordinated for sampling the ocean (Leonard et al. 2007, 2010). The glider's speed is generally faster than ocean currents, but there are situations where it is of the same order of magnitude, and the ''path planning'' problem has been investigated for details on a wide range of single glider missions or glider fleet missions. The simplest situation (reaching a given waypoint) generally reaches simple conclusions, such as ''in a strong adverse current, steer to rapidly cross the current while making up ground where the currents are weak or favorable'' (Davis et al. 2009, p. 186). So, if the ocean currents are known, such simple rules allow for determining if a path is feasible. Based on this rule and additional constraints from the vehicle performances, more complex missions can be planned. Once metrics have been established, one can even include the complex search of optimal paths for several gliders included in a heterogeneous marine observing network (Alvarez et al. 2007). Willcox et al. (2001) have investigated how the limited speed and the battery endurance can limit the performance of generic AUVs to survey oceanic phenomena. Their paper efficiently established a survey tool allowing for solving the trade-off problem between

energy consumption, survey area, and sampling resolution. However, little focus is put on the parameter statistics of the oceanic fields to be surveyed. In a similar oceanic context, Davis et al. (2009) have shown how to control a given ''fixed track'' network while trying to optimize an observing skill locally and globally in the surveyed region. Their method provides an algorithm showing how the optimal network can be maintained in real time depending on the actual current speeds.

The assimilation of glider data in an operational ocean forecasting model has also been used to investigate the efficiency of a single glider repeat section (Dobricic et al. 2010) or of glider networks embedded in operational observing systems (Oke et al. 2009). For obvious logistical reasons, near-coastal current environments have been preferably considered up to now. No general conclusion can be drawn from these experiments, because the skill of the assimilated observations strongly depends on the metrics used and the local particularities of the current system.

Sampling strategies using fixed or mobile platforms (moorings or AUVs) have already been developed for the particular problem of the ocean lateral flux estimate. Zhang et al. (2010) developed a method for analyzing the estimation error, for each type and density of network, and designed the sampling strategy.

In this paper, we focus on the performances of a network of gliders in sampling accurately a realistic mesoscale field of eddies and filaments with an Observing System Simulation Experiment (OSSE) approach. The main objective is to demonstrate that statistics can determine the optimal number of gliders needed to survey a chunk of the ocean at mesoscale with a relatively simple topology of the glider array, such as a ''double comb'' array. A double-comb network can be described as a fleet of gliders flowing parallel to each other, separated by a fixed interval in the direction perpendicular to flow, crossing an area from one side to the other, with every other glider flowing in the opposite direction on parallel trajectories. When each glider reaches the aimed boundary, it reverses course.

The paper is organized as follows. In section 2, we present the glider simulator used to sample a modeled environment, which includes a new path planning algorithm used by the glider itself with onboard processing. Section 3 presents the oceanic modeled environment based on an idealized rotated double-gyre experiment performed at a very high spatial and temporal resolution in order to have a good representation of the mesoscale structures and of realistic ocean situations. This section also presents the topology of the glider network to be optimized and the multiscale objective analysis method used to interpolate the sampled data. Section 4 presents the OSSE itself, which focuses on the reconstruction of the temperature field with several gliders' fixed networks and their corresponding skill. The mesoscale structures obtained by the optimal network are compared with the structures of the original simulation. In this section, the optimization problem is set and the three metrics used to define an analysis skill evaluation as a function of the number of gliders are defined. Before concluding in section 6, section 5 gives the optimal solution and discusses the results in view of their application to an actual in situ experiment.

2. Description of the "glider simulator" OPAGLI

The OPAGLI ''glider simulator'' (B. L'Hévéder et al. 2006, unpublished manuscript) is implemented in the offline tracer module of the OGCM Nucleus for European Modelling of the Ocean (NEMO; Madec 2008). The latter provides the interface between the glider simulator and the files containing the stored outputs of the OGCM simulation. With a few configuration parameters describing the glider fleet and their missions and the 3D time series of the temperature T, salinity S, and currents along the gliders trajectories, the simulator models the flights of gliders, vertically governed by the buoyancy of the modeled oceanic environment, horizontally influenced by the oceanic currents, and their missions defined by lists of waypoints to go through. The outputs of the simulator are the kinematics of each glider (trajectory and velocity) and all the OGCM prognostic variables [T and S, velocity, turbulent kinetic energy (TKE)] sampled along each trajectory.

This glider simulator is independent of the type of glider (Slocum, Spray, Seaglider) and can be adapted, giving appropriate parameters values. It has the basic functionalities of the software on board real gliders.

a. Dynamical model of a glider flight

The glider flies along a sawtooth trajectory between the maximum and minimum target depths, with specific dive/ascent angles. Along the up and down gliding paths, the glider trajectory is calculated by integrating the glider velocity relative to the water, due to its buoyancy engine, in addition to the ambient fluid velocity due to the oceanic currents. The glider velocity is modeled with a simple static equilibrium between the net buoyancy, which is controlled by the ballast of the glider, the lift, and the drag acting on the surface of the glider (Fig. 1). Because of the slow motion of this vehicle and the very laminar flow around the hull, the acceleration can be neglected with a very good approximation, even during the up and down inflexion phases of the flight.

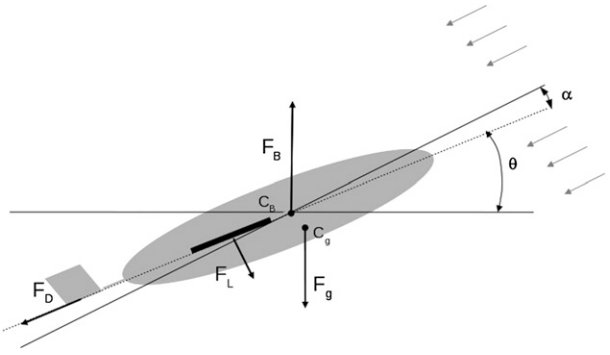

FIG. 1. Schematic representation of the glider during the ascent, forces, and angles definition. Forces applied on the glider are the buoyancy F_B, the gravity F_g, the lift F_L, and the drag F_D. The glider is flying along the glide angle, equal to the sum of the pitch angle theta and the angle of attack alpha.

This equilibrium, projected on the upward vertical, can be written as

$$F_B - F_g - \sin(\theta + \alpha)F_D - \cos(\theta + \alpha)F_L = 0 \quad \text{with} \quad (1)$$

$$F_B - F_g = g\Delta m(T, S), \quad (2)$$

where $\Delta m(T, S)$ represents the net buoyancy of the glider, which depends on $\rho_w(T, S)$ (the density of the local ocean water); the weight (mg L^{-1}); and the varying volume of the glider. The volume of the glider varies with the buoyancy engine and with the local T and pressure P, following this equation:

$$\Delta m(T, S) = \rho_w(T, S)V_{\text{gl}}(T, S)[1 - \chi P + \alpha_T(T - T_0)] + \Delta V_P - m_{\text{gl}}, \quad (3)$$

where V_{gl} stands for the glider's volume at the atmospheric pressure and at $T_0 = 20°C$, ΔV is the glider's volume change, χ is the compressibility hull coefficient, and α_T is the thermal expansion coefficient of the hull. Typical values for an aluminum hull have been used in our simulations with $\chi \sim 3 \times 10^{-5}$ bar^{-1} and $\alpha_T \sim 6.9 \times 10^{-5}$ °C^{-1}.

Following Graver et al. (2003), the drag is parameterized by

$$F_D = \frac{1}{2}\rho_w C_d(\theta, \alpha)S_w U^2, \quad (4)$$

where C_d is the drag coefficient, dependent on the pitch angle θ and on the angle of attack α (in this experiment, $(1/2)\rho_w C_d S_w = 4$ for $\theta = 17°$ and $\alpha = \pm 3°$); S_w is the wing surface area; and U is the glider velocity through water. The projection of Eq. (1) on the glide path can be written as

$$g\Delta m(T, S)\sin(\theta + \alpha) - F_D = 0. \quad (5)$$

Using Eq. (5) and the drag parameterization (4), the velocity module U can be computed, given the pitch angle and the angle of attack, considered constant in absolute value in our model. Finally, the vertical and horizontal components of the glider velocity are derived following

$$u = w\tan(\theta + \alpha). \quad (6)$$

The ambient fluid velocity due to the oceanic currents is provided by the OGCM longitudinal, meridional, and vertical velocity fields. They are interpolated at the glider position with a second-degree Lagrangian polynomial interpolation and at the integration time with a linear temporal interpolation between two consecutive OGCM time steps.

The glider position is integrated, given the total velocity, using a second-step Runge–Kutta scheme with a constant time step that gives a good vertical sampling of the ocean, generally finer than the model vertical resolution.

b. Vertical glider trajectory parameterization

The glider dives from the water surface, flies down along slightly inclined paths (the pitch angle goes from 15° to 30° to the surface) to its maximum depth (depending on the glider model, it is a few meters from the bottom greater than ~15–100 m or the maximum pressure limit—typically about 100, 200, 1000, or more recently even 6000 m). Then, it rises along a similar inclined path to the surface or minimum target depth in case of multiple yos. A change in the piston pump or oil bladder volume ΔV_p, activated by the glider engine, creates successively negative and positive buoyancy. The glider moves on a sawtooth pattern, gliding downward when denser than the surrounding water and upward when buoyant. In the glider simulator, the sign of the volume V_p is changed when the glider reaches its maximum or minimum depth, to simulate the action of the engine activating the piston/oil bladder in the real glider.

As in the software on board a real glider, a simulated altimeter is used to estimate the distance between the current position of the glider and the ocean bottom. The glider is prevented from overstepping a given parameterized distance from the ocean bottom. Between two successive surfacings, the glider can perform several yos (corresponding to one descent and ascent). The main difference between the glider simulator and a real glider concerns the pitch and heading during the downward and upward phases, which have constant values in the simulator, whereas in the reality they can vary slightly

around these constant values, even when actively controlled by the glider software.

c. Horizontal glider trajectory parameterization

The horizontal glider trajectory is supposed to go through a list of waypoints (latitude/longitude) defined by the pilot: once one waypoint is reached by the glider (i.e., the glider is at a minimum distance from the waypoint, typically 0.5 km), the latter aims to reach the following waypoint in the list provided by the user. Under water, the glider uses dead reckoning at each time step. The glider periodically surfaces to simulate communicating data and instructions and obtaining GPS fixes. During the surfacing, any difference between dead reckoning and GPS fixes, attributed to ocean currents, is stored and will be used to correct the glider heading. As long as it lies at the water surface (time needed for simulated GPS fixes and communications), the glider drifts freely with surface currents.

Because of the limited glider velocity (0.2–0.4 $m\,s^{-1}$) comparable to that of ocean currents and much lower to that of strong boundary currents, the ideal trajectory linking linearly one waypoint to the following one is difficult to achieve by the glider and therefore likely not optimal. Its trajectory is easily deviated by oceanic currents, and some geographical points, located in the vicinity of strong oceanic currents are difficult—even sometimes impossible—to reach. So, the chosen strategy is first to fly as close as possible to each waypoint, reaching at least a point located at a minimum parameterized distance from the waypoint. Second, to get the most rapid trajectory between two consecutive waypoints, ''heading correction'' methods, using the average oceanic current over dives estimated by the glider, are implemented in the simulator. This estimated average current corresponds to the average of the horizontal ocean currents along the sawtooth trajectory.

The glider trajectory depends on the ocean currents and buoyancy and on the parameters specified by the user—the number of yos between two surfacings, the maximum depth to achieve, the buoyancy changes of the glider—and finally on the heading direction, which can be chosen to optimize the trajectory. There is a single heading direction held fixed between at least two surfacings. This single heading direction is selected in a different way, and therefore it will be different, according to the choice of the heading correction method. In the default case, the glider flies without heading correction, and the heading direction is simply estimated by aiming at the waypoint from the actual glider position. In the two heading correction methods described in the appendix, the heading direction is no longer the waypoint direction but a direction supposed to compensate for the oceanic currents. These heading correction methods improve considerably the capability of the gliders to cross very strong currents, and their velocity along the crossing of the domain, in a way comparable to other path planning methods (Garau et al. 2005, 2006; Davis et al. 2009).

d. Parameter values used in this experiment

In the OSSE performed in this study, the same flight configuration is taken for all the gliders: a dive constituted of one ''yo'' from the ocean surface to 1000 m, with a pitch angle of 17°; an attack angle of ±3°; and a stay of 10 min at the surface between two dives. Since the simulated gliders evolve in a region with particularly strong currents, we use a 40 $cm\,s^{-1}$ glider speed relative to the water. It corresponds to the maximum glider speed that can be achieved with a Slocum glider, using the entire volume of the pump: 250 cm^3. This glider speed is inside the realistic range (20–40 $cm\,s^{-1}$).

The steering strategy is based on two principles: the use of the heading correction from Lekien et al. (2008) and the waypoints strategic position. In this heading correction method, described in the appendix, the heading is adjusted to counteract completely the deviation induced by the flow, when it is possible. Using this navigation algorithm, the simulated gliders are able to cross a domain with strong currents without any steering intervention. This is also facilitated by the second principle: the waypoints are fixed 200 km farther than the domain boundary, and the gliders have to reach a point situated at 210 km from the waypoint. This allows the gliders to turn back at a point located around the domain boundary, inside an interval of [−60, 60] km to the left/right of the point situated on the boundary and aligned to the aimed waypoint. It gives a large flexibility to the shape of the trajectories, enabling the gliders to cross strong currents. Using these waypoints, the gliders actually attempt to maintain a constant heading, rather than fit into a narrow navigation corridor.

Concerning the trajectory integration time steps, the OGCM temperature, salinity, and velocity fields have a 2-day temporal resolution and the glider position time step is taken at 30 s.

3. The numerical experiment

a. The control simulation of the oceanic domain

The gliders are sampling the ocean at very high spatial resolution: a few meters on the vertical and a few kilometers on the horizontal, and the corresponding temporal resolution goes from seconds (vertically) to hours (horizontally). The gliders are very efficient at capturing (sub)mesoscale structures (Pietri et al. 2013) and their

spatiotemporal evolution. To simulate as realistically as possible the sampling of a glider network, a numerical experiment able to reproduce mesoscale structures had to be used. In numerical models, mesoscale eddies emerge when the horizontal resolution is of $O(10\,\text{km})$, while a resolution of $O(1\,\text{km})$ is necessary to capture submesoscale turbulence (Siegel et al. 2001). The objective of the GYRE experiment was precisely to model mesoscale and submesoscale structures using an OGCM. With this aim in view, a series of simulations was performed with increasing horizontal resolution, the highest being 2 km ($^1/_{54}°$ horizontal resolution). In the latter, the numerical models observed "the emergence of energetic submesoscale filaments and the explosion of mesoscale eddies, with the increase of the eddy kinetic energy" (Lévy et al. 2009, p. 14). Therefore, this simulation seemed appropriate to conduct this study.

In the GYRE experiment, for the sake of simplicity, an idealized rotated double gyre is modeled. The domain geometry is a rotated, closed rectangular basin on the beta plane (Fig. 2), bounded by vertical walls and by a flat bottom (after Hazeleger and Drijfhout 1998). The circulation is forced by analytical zonal winds and buoyancy fluxes that vary seasonally and with latitude. There are 30 z-coordinate vertical layers, and the horizontal resolution is of $^1/_{54}°$ (about 2 km). The NEMO primitive equation model (Madec 2008) is used. The description of the parameterization of diffusion, advection, and lateral conditions used in this simulation is done in Lévy et al. (2010); the available output fields are averaged over 2 days.

A reasonable experiment with a glider fleet aiming to characterize accurately the mesoscale field would be able to capture the weekly variability (typical of mesoscale evolution) of a sufficiently large region (hundreds of kilometers) to show interactions between the large-scale flow and the mesoscale features, as well as eddy–eddy interactions.

An anisotropic region of 400 km × 600 km was selected, centered on the latitude 34°N and on the longitude 77.5°W, in a very energetic part of the idealized Gulf Stream current (Fig. 2). For this experiment, a monthly period, corresponding to the typical duration of a research vessel cruise, allowing the deployment and recovery of all the gliders, was chosen.

Figure 3 shows the complete series of the 2-day mean temperature field at 100-m depth. The large-scale frontal structure, the mesoscale features, and their temporal evolution during the 40 days of the simulation can be well identified. A front materializing the idealized Gulf Stream current separates warm waters in the south from cold waters in the north. During the 4-week period, the position of the front changes and a warm ring detaches

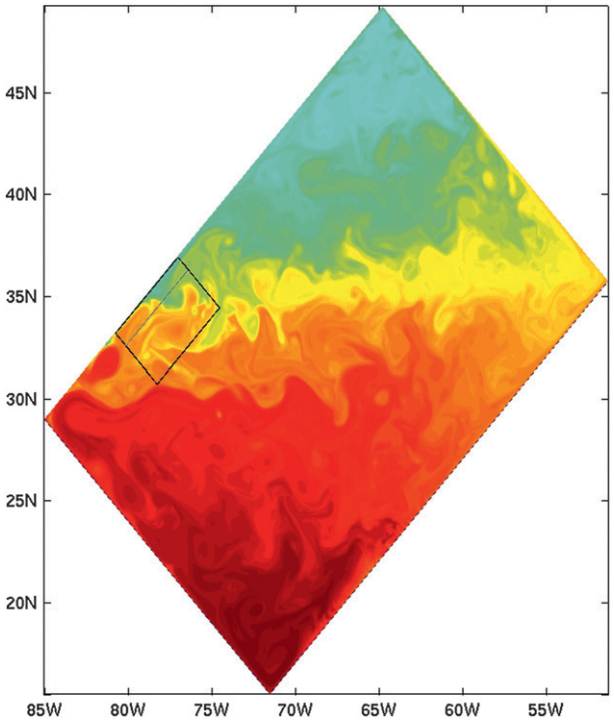

FIG. 2. Snapshot of the 100-m-depth horizontal temperature field in the GYRE experiment. The black frame indicates the 400 km × 600 km region selected for the OSSE. The gray line parallel to the northwestern boundary of the OSSE domain delimits the vertical section plotted in Fig. 8.

and propagates to the north. At the scale of this area and of the week, there is a significant spatiotemporal variability.

In this simulation (comparable to the midlatitude North Atlantic), the deformation radius is about 60–80 km and the mesoscale activity is very well resolved spatially. Simple mesoscale statistics in the model are compared to the observations of the Gulf Stream current (Berezutskii et al. 1991). The Gulf Stream current dimensions (100 km wide and 800–1200 km deep) are well represented in the model. The Gulf Stream is the fastest near the surface, with typical maximum velocities of $2\,\text{m s}^{-1}$. In the model, the velocity is too low in the 500 surface meters, with a maximum velocity range of 0.7–$1.3\,\text{m s}^{-1}$ against $1.22\,\text{m s}^{-1}$ in the observations (Fig. 4; Berezutskii et al. 1991). Then, below 500-m depth, the current velocity decreases with depth is well represented in the model, with a maximum velocity of $0.5\,\text{m s}^{-1}$ in the Gulf Stream. The spatial standard deviation of the current velocity is $0.2\,\text{m s}^{-1}$ at the surface and decreases to $0.1\,\text{m s}^{-1}$ below 200 m.

In the observations, the main current meanders breaking off the stream create rings, which are usually between 50 and 200 km in diameter. The warm and cold rings

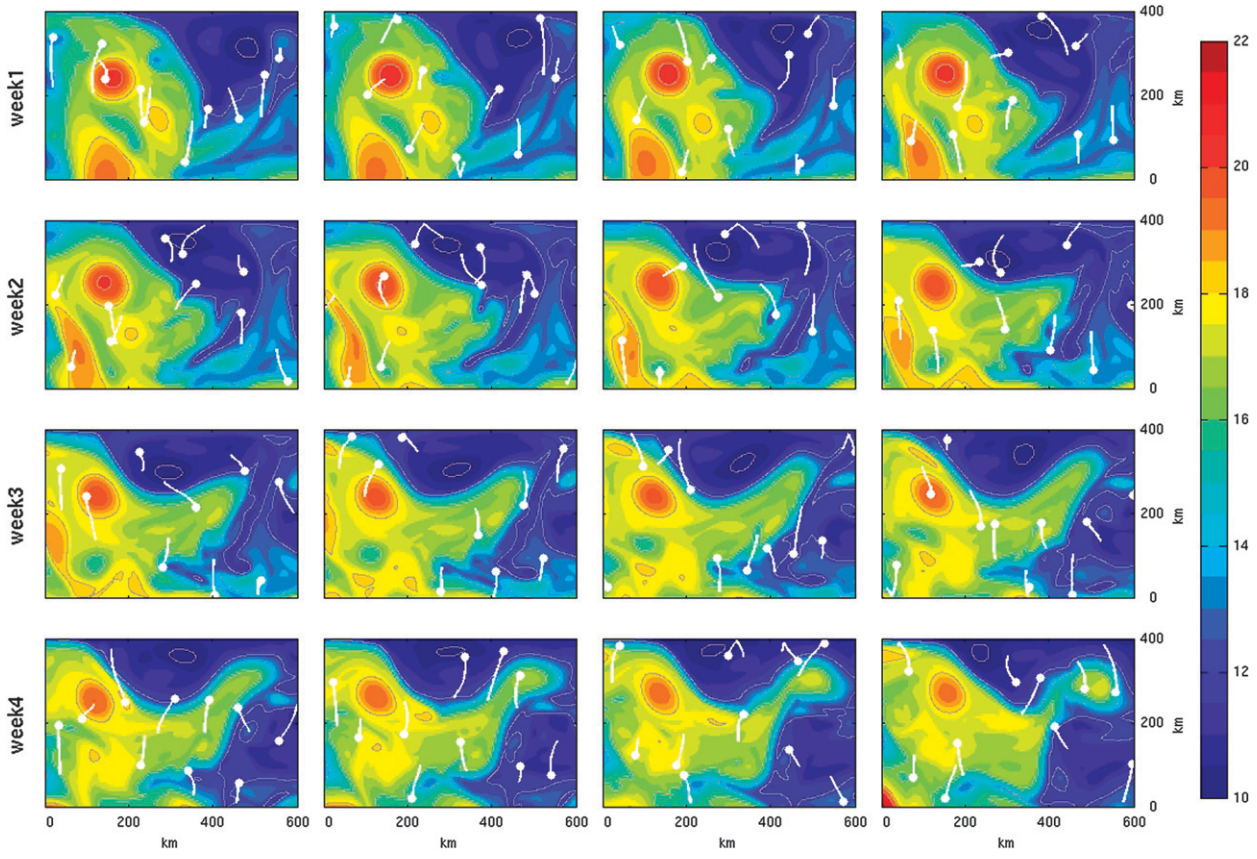

FIG. 3. Horizontal temperature field at 100 m of the control simulation (2-day mean), and trajectories of 10 gliders (white plots) during the two corresponding days of the experiment. Gray contours stand for 2°C intervals. Each "week" of the simulation (horizontal lines) are composed of four groups of 2 days (vertical columns).

present in the domain are well dimensioned (between 100 and 150 km in diameter), with realistic rotational velocities of about 1 m s^{-1}.

Across the front, the observed temperature change of 5°C (Berezutskii et al. 1991) is well reproduced in the model. In the model, the front is well represented in the 400 surface meters, with temperature ranges of 12°–20°C.

In conclusion, the model recreates statistically quite well a portion of the midlatitude open ocean. The shortcoming is the underestimation of the velocities in the 500 surface meters, but they remain characteristic of strong currents.

b. *The glider network's topology*

The deployment of a network of gliders organized in a double-comb pattern is chosen. As already mentioned in the introduction, a double-comb pattern can be described as a fleet of gliders flowing parallel to each other, separated by a fixed interval in the direction perpendicular to flow, crossing an anisotropic area (across front) from one side to the other, with every other glider flowing in the opposite direction on parallel trajectories. When each glider reaches the aimed boundary, it reverses course.

Different glider network patterns have been tested in the real ocean or in numerical simulations. Two main cases can be distinguished depending on whether a control strategy is adopted. Without a control strategy, most of the time, the gliders fly along a repeated section (Castelao et al. 2008; Bouffard et al. 2010; Dobricic et al. 2010; Pietri et al. 2013). The repeated section remains the more efficient shape for the estimation of oceanic quantities like velocities and lateral fluxes. Hodges and Fratantoni (2009) set five gliders in a fixed position to form a synthetic moored array. In the Everybody's Gliding Observatories (EGO) experiments, different shapes of the glider network have been tested, such as arranged crosswise or squarewise (Testor et al. 2007, 2010; L'Hévéder et al. 2009). Leonard et al. (2007) have tested a comb array with five gliders and five other gliders traveling around approximately trapezoidal racetracks in the AOSN experiment.

In addition, more sophisticated glider network topologies have been developed, using a control strategy

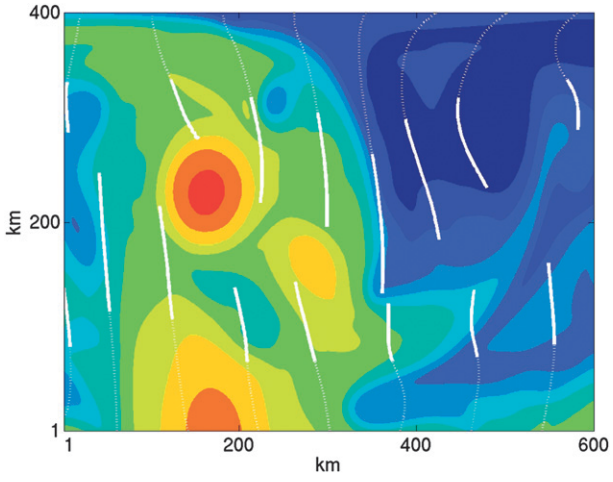

FIG. 4. Horizontal temperature field at 100 m of the control simulation and trajectories of a 16-glider fleet (white plots) during days 3 and 4 of the experiment.

to optimize the glider paths in oceanic current fields (Garau et al. 2005, 2006); to optimize the combined network topology with a network composed of drifting profiling floats and gliders (Alvarez et al. 2007); or to control automatically a fleet of gliders, maintaining a prescribed intervehicle spacing (Leonard et al. 2010).

In this study, the objective is to propose a glider network that is easy to set up (without a control strategy), that is the most autonomous as possible (no need for operational intervention for the steering), and that optimizes the coverage of the region in terms of mapping errors. The key advantages of the double-comb pattern are first, each glider is alone on its trajectory, so that it does not carry the risk of two gliders meeting at the same place because of a slowing down due to an eddy, for example; second, the ideally linear glider trajectories can be a bit curved without too much impact on the sample coverage, which is less true when using a square-wise or trapezoidal pattern; finally, the deployment of this type of network requires only a few days of ship time and does not require human intervention for steering during the 1-month experiment.

Figure 4, where the trajectories of a network of 16 gliders are plotted during days 3 and 4 of the simulation, gives an overview of the network topology. One glider heads toward the northwestern boundary of the domain and the following one heads toward the opposite boundary. Once the aimed boundary of the domain is reached, they go back and forth along the northwest–southeast section during 40 days. Figure 3 shows the complete series of the 2-day mean temperature field at 100-m depth, with the trajectories of a fleet of 10 gliders, during the two corresponding days of the experiment. The gliders look well distributed in space and time. Moreover, the deviation of the gliders' trajectory by the currents is also well illustrated.

The objective of this study is to find the optimum number of gliders needed to reconstitute a quasi-synoptic image of the mesoscale variability at a weekly time scale. Therefore, a sensitivity study was performed with different glider fleets, ranging from 2 to 30 gliders, with a network horizontal resolution of 300–20 km.

c. *Objective analysis approach*

The gliders sample the region during one month, and the collected data can be used to get weekly synoptic snapshots of the upper 1000 m of the ocean. The gliders are equipped with sensors to measure tracers (temperature, salinity, and also oxygen, fluorescence, and turbidity), and the objective here is to reconstitute the weekly three-dimensional tracer fields with an objective analysis method in a similar way as it could be done with actual data. The methodology, applicable to any type of tracer, will be illustrated here with the temperature field only.

An objective mapping of the glider data is done to the mesh grid of the ocean model, in order to get a regular mapped field and to be able to test the performance of the method by comparing to the original 3D temperature fields of the model. The method is applied to the 2D horizontal fields, for each vertical level of the model grid and for each midweek date. Then, the four time steps of the 3D field are reconstructed. Following Roemmich (1983), it is assumed that the horizontal tracer field can be decomposed into two principal scales: the first being a very large scale over which properties are slowly varying, and the second is a much smaller scale that is just resolved by classic hydrography. Moreover, the temporal variations of the smaller-scale structures are taken into account, adapting the method developed by Böhme and Send (2005). In their study, they use an objective mapping method taking the temporal and spatial variations in water mass properties into account, in order to build a set of calibrated salinity data, with corresponding uncertainties. In our study, the following objective analysis method is used: a first mapping set representing the mean state at a large scale of the oceanic structures is computed with the raw glider data. Then, this first mapping set is subtracted from the raw glider data, giving a set of residuals, still containing the small time and spatial scales. Second, a second mapping set is computed with the set of residuals for each midweek date of the simulation. It contains the small time- and spatial-scale information. As in Böhme and Send (2005), the final estimate of the glider data analysis is the sum of the two mapping sets, containing together large and small components.

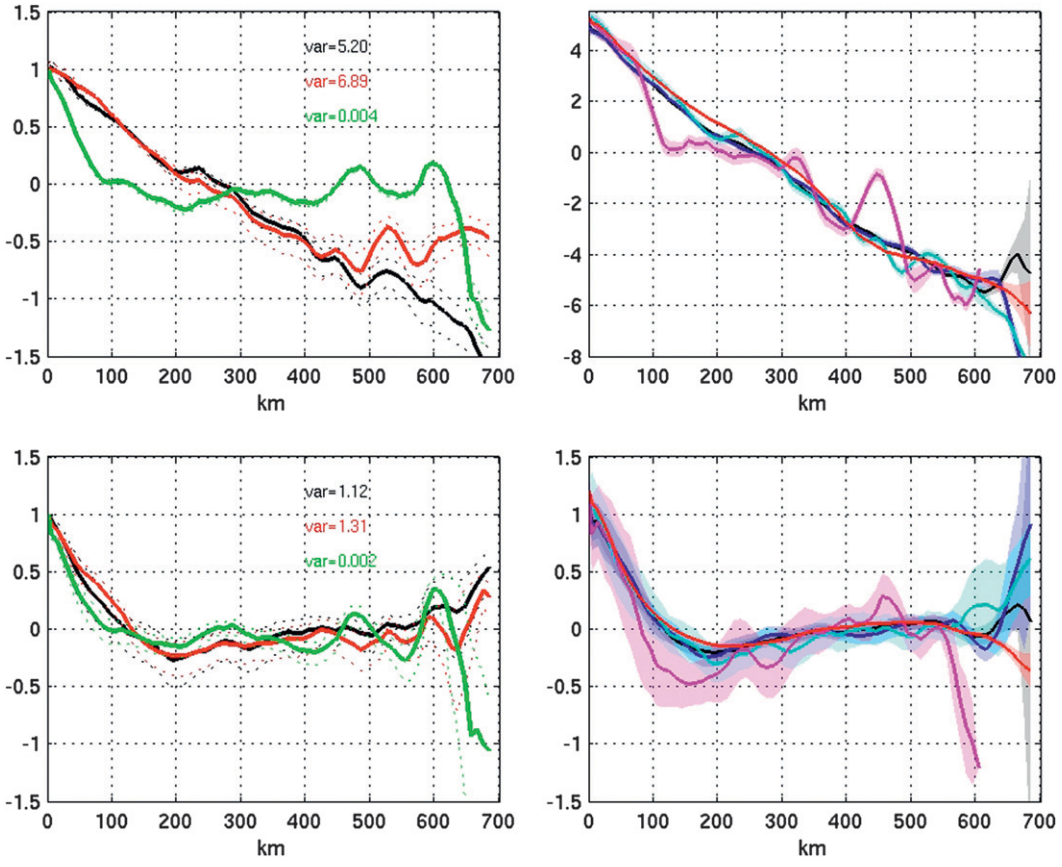

FIG. 5. Spatial variograms of the gliders' data. (left) Spatial variograms of a 10-glider fleet, computed at the surface (black line), at 100-m depth (red line), and at 500-m depth (green line), and normalized by the spatial variance at the corresponding level (values noted in the top-right corner). Dotted lines show the 95% confidence level according to a two-sided *t* test for each depth. (right) Spatial variograms of a 30- (black line), 20- (dark blue line), 10- (light blue line), 5- (magenta line) glider fleet, and of the model data (red line) are computed at the surface. Shaded regions correspond to the 95% confidence level according to a two-sided *t* test. (top) Raw set of data. (bottom) Large-scale structures have been filtered.

The characteristic large and small spatial scales and the temporal scale are estimated from variograms computed with the glider data. Consequently, this method is applicable to a real experiment, where the only available information is glider data.

The large scale has been estimated from the spatial variograms of the raw glider surface data, computed with different glider fleets (Fig. 5, top-right subplot). For more than 10 gliders, the variograms exhibit a shape characteristic of a front structure: a straight line with a decreasing slope, crossing zero at about 300 km. It corresponds to a large scale of about 300 km, characteristic of a front, which appears clearly on the horizontal section of the temperature field (Fig. 3). To get an estimate of the different spatial scales represented in the glider fleet sampling, as a function of the number of gliders used in the network, the spatial variogram of the surface temperature fields in the control simulation has also been plotted in red on the top-right subplot (Fig. 5). The curve is very close to those obtained with more than 10 gliders, showing that, from this number of gliders, all the spatial scales are well captured, with a variance very close to that of the control simulation. With five gliders, the front structure is not that well represented, and a cutoff can be observed at about 120 km, corresponding to the spatial resolution of the glider spacing, with gliders spaced about 120 km (the domain width, 600 km, divided by five gliders). All along the plot, variance peaks appear for each multiple of 120 km. It demonstrates that in this case, the spatial resolution, by construction inhomogeneous in one direction of the domain, is insufficient. In the top-left subplot of Fig. 5, spatial variograms of the 10-glider fleet have been plotted for different depths. The variograms have been normalized, because the variance is lower by a factor 10^{-3} at depth. The 100-m and surface variograms are very similar, unlike at 500 m, where the front is much weaker (as can be seen on the vertical section of Fig. 8).

The large-scale field is oversampled by the glider data, constituted by a 40-day temporal series of about 3000 measurements per glider per day (corresponding to a sampling time scale of 30 s). Consequently, for each vertical level, all the gliders' data in the range of ±1.5 m around the level depth are selected, interpolated, and averaged on the horizontal model grid. This selection is done in the complete temporal series, since the large-scale mapping has no temporal component.

In the first mapping set, the covariance is a function of the horizontal separation only and the decay scale is determined by the large spatial scale ($L_1 = 300$ km). The covariance matrix $\mathbf{C}^1_{\text{mg}}$ between the mapping on the model grid and the glider data, and the autocovariance matrix $\mathbf{C}^1_g$ of the glider data can be modeled as

$$\mathbf{C}^1_{\text{mg}}(i,j_g) = (1-\epsilon)\exp\left[-\frac{1}{2}\left(\frac{D_{i,jg}}{L_1}\right)^2\right] + \epsilon\delta(i,j_g) \quad \text{and} \tag{7}$$

$$\mathbf{C}^1_g(i_g,j_g) = (1-\epsilon)\exp\left[-\frac{1}{2}\left(\frac{D_{ig,jg}}{L_1}\right)^2\right] + \epsilon\delta(i_g,j_g), \tag{8}$$

where $D_{i,j}$ denotes the distance between the two points i and j, δ stands for the Dirac function, and ε is the relative variance error fixed at 0.05. A mean basinwide field is estimated on the model grid points for each vertical level. Then, the estimated values of the 3D field obtained in the first mapping step are subtracted from the glider data, previously interpolated on the horizontal model grid for each model time step and vertical level, giving the set of "residuals."

Then the second mapping set is computed, mapping the set of residuals to the model grid points using covariances $\mathbf{C}^2_{\text{mg}}$ and $\mathbf{C}^2_g$, which are functions of the temporal and small spatial separation. The decay scale is determined by the small spatial scale (L_2) and the temporal scale (τ):

$$\mathbf{C}^2_{\text{mg}}(i,j_g) = (1-\epsilon)\exp\left\{-\frac{1}{2}\left(\frac{D_{i,jg}}{L_2}\right)^2 - \frac{1}{2}\left[\frac{(t_i - t_{jg})}{\tau}\right]^2\right\} + \epsilon\delta(i,j_g) \quad \text{and} \tag{9}$$

$$\mathbf{C}^2_g(i_g,j_g) = (1-\epsilon)\exp\left\{-\frac{1}{2}\left(\frac{D_{ig,jg}}{L_2}\right)^2 - \frac{1}{2}\left[\frac{(t_{ig} - t_{jg})}{\tau}\right]^2\right\} + \epsilon\delta(i_g,j_g), \tag{10}$$

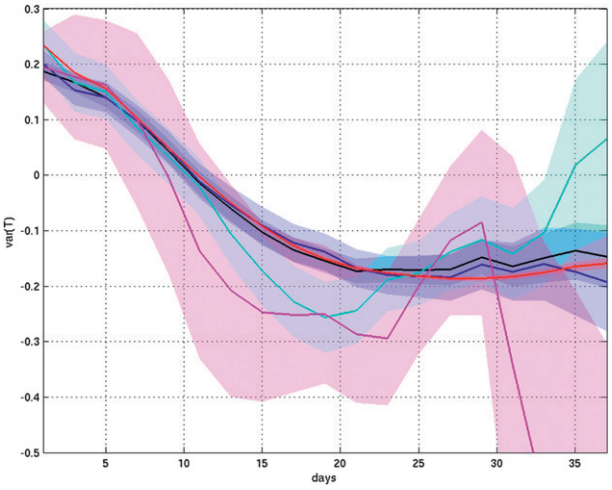

FIG. 6. Temporal variograms of the gliders' data for a fleet of 30 (black line), 20 (dark blue line), 10 (light blue line), 5 (magenta line) gliders, and of the model data (red line), computed at the surface. Shaded regions correspond to the 95% confidence level according to a two-sided t test.

where ε is the relative variance error fixed at 0.05. The small spatial scale and the temporal scale are estimated from variograms computed with the glider sampling data. The small spatial scale is estimated from the spatial variograms of the residuals, computed with the surface data of the different glider fleets (Fig. 5, bottom-right subplot). The spatial variogram of the control simulation, computed with the surface temperature anomaly fields to the 40-day temporal mean, has also been plotted (red curve). Because a first analysis of the mean spatial field, averaged over the entire duration of the simulation, has been removed, the large spatial scales have been removed and the small spatial scales emerge. All the plots exhibit the same shape: a Gaussian function with a decorrelation spatial scale of 120 km, corresponding to a decay spatial scale of about 85 km, except for five gliders where it is instead 55 km. It corresponds to mesoscale structures with a characteristic spatial scale close to the deformation radius of the area. This result is consistent for deeper depths, as shown in the bottom-left subplot of Fig. 5, where the spatial variograms of the residuals are computed for three different depths for a 10-glider fleet. For more than 10 gliders, the very good consistency between the results obtained with the glider-sampled data and with the control simulation data emphasizes the efficiency of the glider networks to sample the domain at all spatial and temporal time scales. Given this results, the small spatial-scale value used in the objective analysis is fixed at $L_2 = 85$ km.

Temporal variograms of the residuals are also computed with the surface data of different glider fleets and with the control simulation fields (Fig. 6). For more than

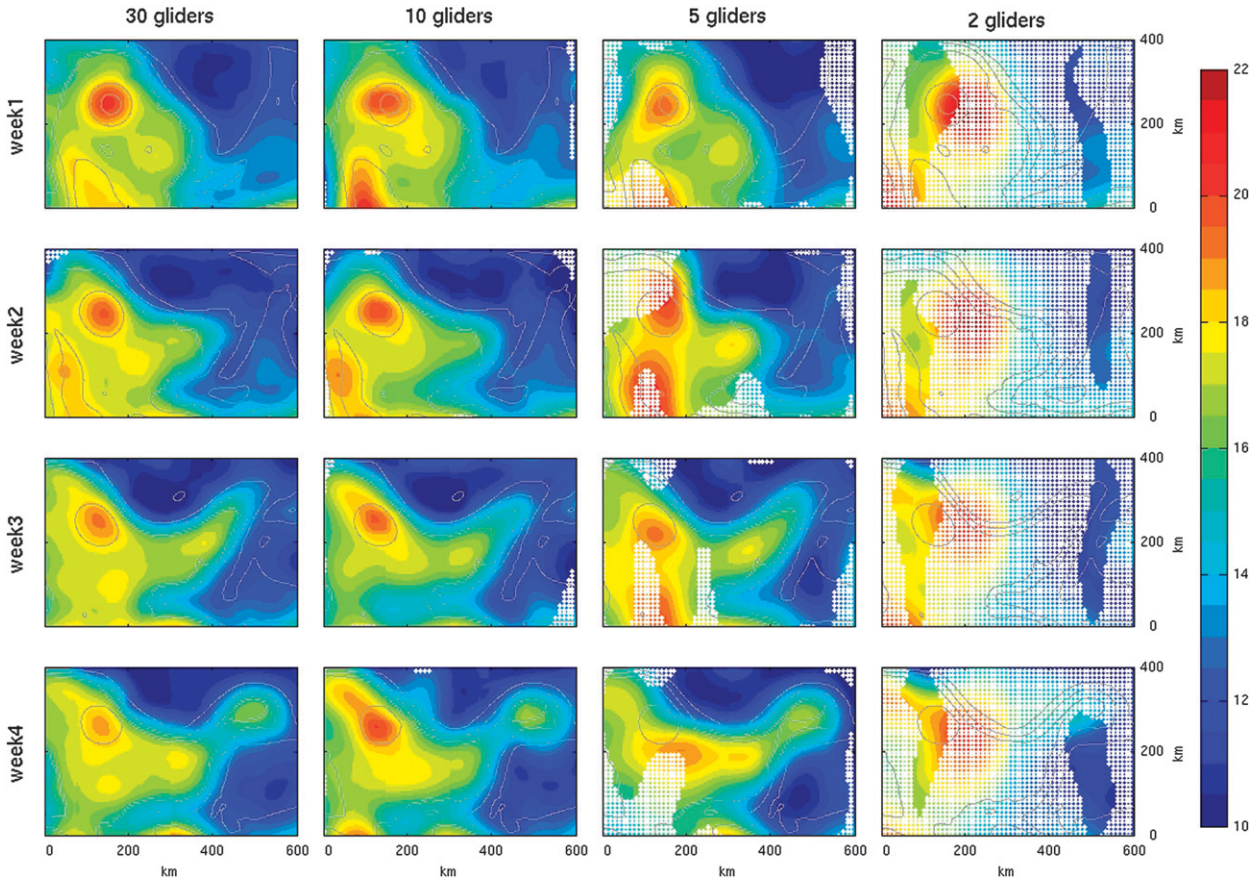

FIG. 7. Colors show horizontal temperature fields of the glider data analysis at 100-m depth, performed with a 30-, 10-, 5-, and 2-glider fleet. Gray contours (with 2°C intervals) show corresponding control temperature fields averaged over the corresponding week. Gridded area correspond to the points whose analysis variance error is greater than 5% of the total variance.

10 gliders, as for the control simulation, the temporal variograms give a decorrelation time scale of about 10 days, corresponding to a decay time scale of $\tau = 7$ days. This value is taken as the temporal time scale for the objective analysis. As highlighted for the spatial variograms, a clear boundary appears at 10 gliders.

To complete the description of the methodology, the glider data will be considered in temporal windows of ± 8 days around the dates of the midweek. Therefore, the 4 days preceding and following each week are also used to reconstitute the midweek snapshot—that is why a simulation of 40 days is necessary to reconstitute a quasi-synoptic image at a weekly time scale of 4 weeks of 8 days.

4. Qualitative results and skill evaluation

Around 10 experiments were performed with a 2–30-glider fleet. Then, the gliders' data were analyzed to get three-dimensional temperature fields, for four dates corresponding to the middle of each of the 4 weeks, for each experiment.

a. Qualitative comparison with the control simulation

Figures 7 and 8 enable a qualitative check of how well the glider data analysis of the temperature field agrees with the corresponding field of the control simulation. Figure 7 shows the 100-m horizontal section, while Fig. 8 shows the vertical section situated at 100 km from the northwestern boundary (see Fig. 2). The analysis performed with a fleet of 30 gliders gives a very good reconstitution of the temperature fields (Fig. 7), sticking to the corresponding control fields. The formation of the new anticyclonic eddy and its spreading to the north is very well detected. In the analysis carried out with 10 gliders, the spatial and temporal variability of the horizontal fields are satisfactorily captured. With five gliders, the structures are less well represented and the analysis using only two gliders gives a dipole structure. The shaded area corresponds to the points of the model grid

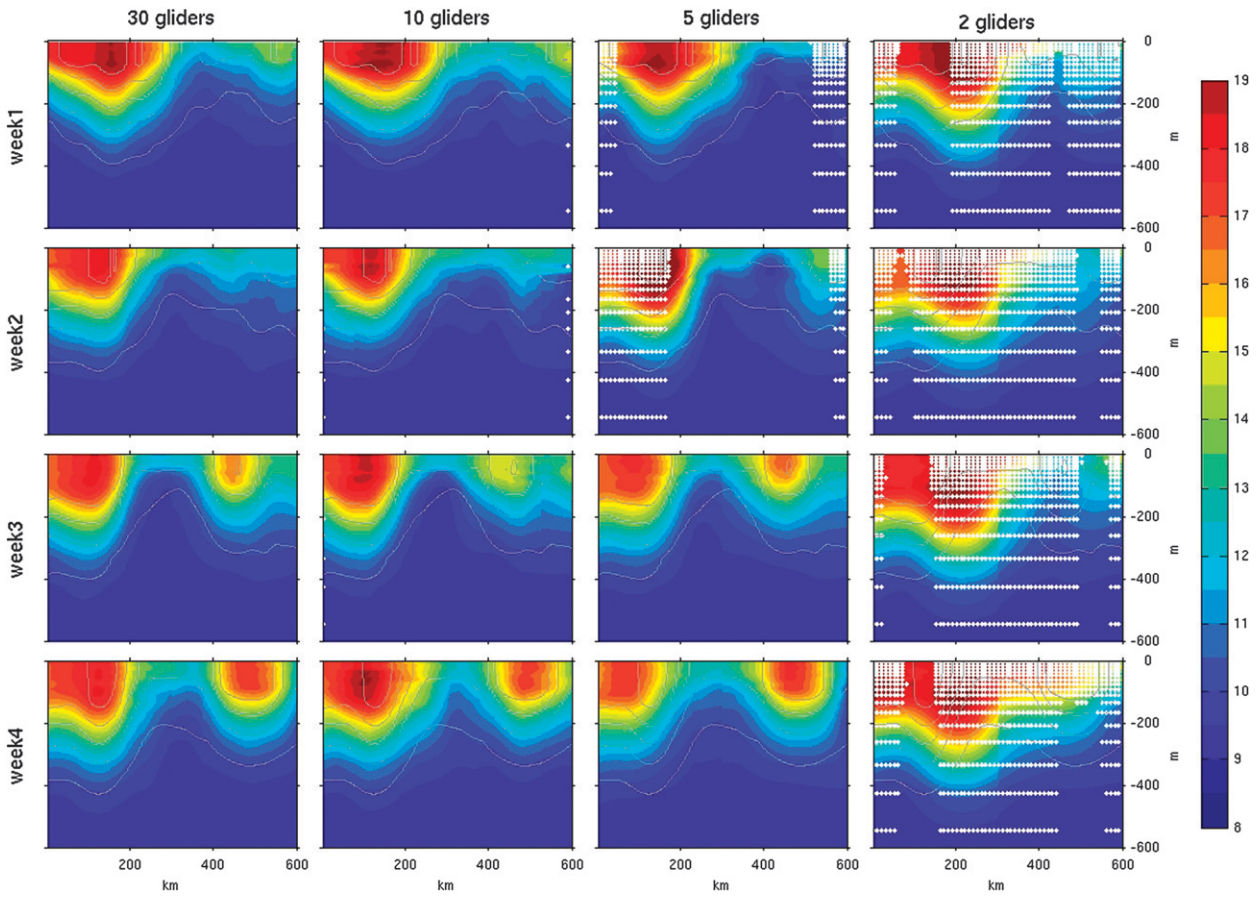

FIG. 8. Colors show vertical temperature fields of the glider data analysis (along the section plotted in Fig. 2), performed with a 30-, 10-, 5-, and 2-glider fleet. Gray contours (with 2°C intervals) show corresponding control temperature fields averaged over the corresponding week. Gridded area corresponds to the points whose analysis variance error is greater than 5% of the total variance.

on which the analysis variance error is greater than 5% of the total variance. With more than 10 gliders, it is very small. With five gliders, the shaded areas are situated on the left/right side of the domain, less sampled by the gliders. In the second week, the amplification and the shift of the two warm eddies situated in the left part of the domain can be explained by the glider data undersampling in the near vicinity of the eddies. With two gliders, the nonshaded areas provide essentially information about the glider positions and their movement during the 4 weeks. In this case, the spatial distribution of the glider data is not sufficiently homogeneous to enable a correct 3D field reconstruction with this objective analysis method.

Considering that the tracers and ocean velocity fields are quite homogeneous below 400 m in the control simulation (because of the idealized domain and forcing), only the upper 600 m of the vertical section were plotted in Fig. 8. The eddies have a deep signature extending to 400 m, but most of the signal is concentrated in the upper 250 m. In the analysis using the 30-glider fleet, the successive steps of the formation of a new anticyclonic eddy are also well captured. Only a small shift of the contours around the front can be observed. For the analysis performed with fleets of 10 and 5 gliders, the temporal variability of the mesoscale structures is well captured; the analysis fields' shortcoming takes the form of an horizontal shift of the two eddies. The analysis using the two-glider fleet does not capture at all the new eddy formation. The shaded points, whose analysis variance error is greater than 5% of the total variance, show the model vertical grid, corresponding to the effective position of these points. With more than 10 gliders, there is no shaded area for this particular section. Again, the weekly evolution of the nonshaded areas gives essentially only an idea of the gliders' movement during the 4 weeks.

By construction, submesoscale structures present in the control simulation do not appear in the analysis fields (both Figs. 7 and 8). Since the aim of this study is to reconstitute a weekly synoptic snapshot of the mesoscale variability, the order of magnitude chosen for the small spatial scale corresponds to the Rossby deformation

radius. The same methodology could certainly be applied to reconstitute submesoscale structures, as the high-resolution sampling of the gliders along its trajectory can effectively capture submesoscale filaments, but it would require substantially increasing the glider network resolution and it is beyond the scope of this study.

b. Objective analysis skill evaluations

Although a visual estimate of the minimal number of gliders required to have a quasi-synoptic image of the mesoscale variability at a weekly time scale gives a value of about 10 gliders in our experiment (Figs. 7 and 8), it is worth defining an analysis skill evaluation as a function of the number of gliders. Three different metrics are used in this paper: root-mean-square (RMS) comparison, spatial pattern correlation (PC) between the glider data analysis and the control fields, and objective analysis (OA) error. With these three metrics, the optimal solution can be determined. It will be defined as the minimum number of gliders for which the removal of one glider in the fleet would increase the average normalized errors of the three metrics by more than 1%.

1) ROOT-MEAN-SQUARE ERROR

An RMS comparison between the glider data analysis and the control fields has been performed as follows: for the different glider fleets and for the 18 vertical levels covering the upper 1000 m of the ocean. For each of the four midweek dates, taken as independent representations of the system, the temperature horizontal fields of the glider data analysis are compared to the corresponding control simulation fields, averaged over the corresponding week. The analysis and control fields are mapped onto the same horizontal and vertical grids, as required for such comparison.

Horizontal normalized RMS errors of temperature $T_{\mathrm{RMS}}(k)$,

$$T_{\mathrm{RMS}}(k)=\left(\frac{1}{n_t}\sum_{t=1}^{n_t}\left\{\frac{\frac{1}{n_i}\sum_{i=1}^{n_i}[\overline{T_M}(i,k,t)-T_G(i,k,t)]^2}{T_w(k,t)}\right\}\right)^{1/2}, \tag{11}$$

are evaluated for each vertical level k, where n_i is the number of grid points at that level; n_t is the number of midweek dates of the experiment; $\overline{T_M}$ is the control model data, averaged over the week; and T_G is the glider data analysis. The RMS error is normalized by a target value $T_w(k, t)$, defined as the temporal temperature variance inside the week in the control simulation. The latter temperature takes a maximum value of about 0.5°C in the upper 100 m, and then decreases with depth. Because the time resolution chosen for the field analysis is a week, the frequencies higher than the week are not resolved using this methodology by construction. Consequently, the aim of the experiment is to get as close as possible to this target value.

The normalized RMS errors do not present any vertical variability. Therefore, the results of the RMS metric, averaged on all the grid points of the control model grid, over the four midweek dates, are plotted in the middle panel of Fig. 9.

With more than 10 gliders, the temperature RMS errors are almost equal to the temporal temperature variance inside the week in the control simulation, giving a normalized value between 1.25 and 1.65. So, a quasi-synoptic image of the three-dimensional temperature field at a weekly time scale is obtained, with errors of the order of magnitude of the temporal variability at frequencies higher than the week. When fewer than 10 gliders are used, the results are more spread out and the errors are larger.

2) SPATIAL PATTERN CORRELATION

The diagnostics computed above provide a metric of the distance between two datasets in terms of the RMS error. However, the error does not contain any information about the spatial structures of the datasets. Information on the similarity of the spatial patterns can be provided by the centered pattern correlation coefficient, as defined in Onken et al. (2007):

$$T_{\mathrm{PC}}(k)=\frac{1}{n_t}\sum_{t=1}^{n}\left\{\frac{[T_M(i,k,t)-\overline{T_M}(k,t)]^t[T_G(i,k,t)-\overline{T_G}(k,t)]}{\mathrm{std}[T_M(k,t)]\mathrm{std}[T_G(k,t)]}\right\}, \tag{12}$$

where $T_{\mathrm{PC}}(k)$ is the centered pattern correlation coefficient for temperature (PC coefficient), correlating the horizontal temperature field T_G of the glider data analysis to the control model one T_M, evaluated for each vertical level k and for the four midweek dates t of the experiment. As for T_{RMS}, T_{PC} is the mean of the four midweek dates, considered here as independent representations of the system.

The PC coefficient can take values between −1 and +1. If the patterns are similar, then T_{PC} is positive, and in case of a perfect correlation, T_{PC} is equal to 1. When it comes to zero, it means that the patterns are not correlated.

In the left panel of Fig. 10, the vertical profiles of the PC coefficient are plotted for temperature. With this metric, two groups of curves emerge, with a limit at about 10 gliders. From 10 gliders, the PC coefficient is

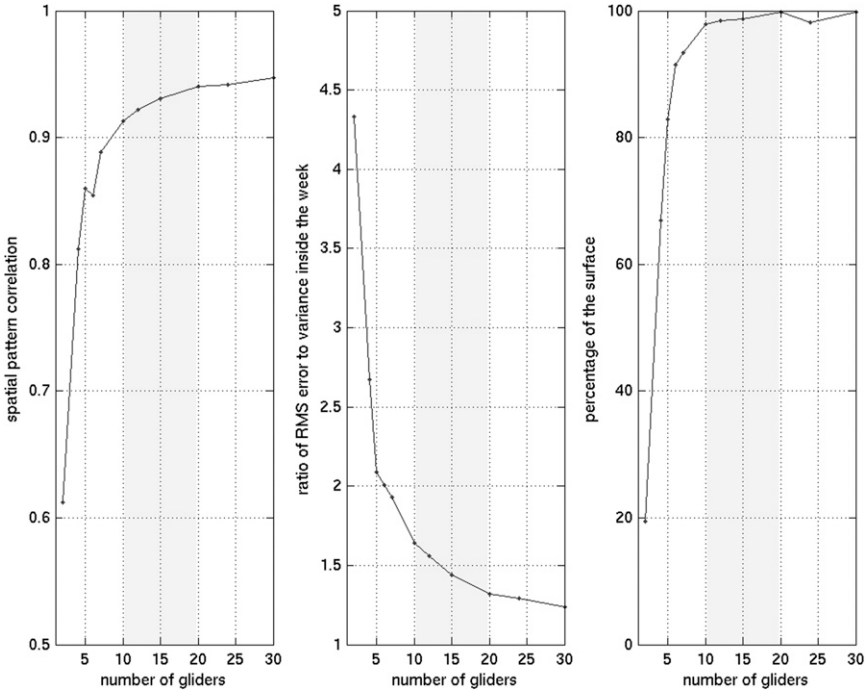

FIG. 9. (left) T_{PC}, (middle) ratio of T_{RMS} to the variance inside the week, and (right) percentage of the surface with an analysis variance error less than 5% of the total variance, averaged over all the grid points and the four midweek dates, as a function of the number of gliders in the fleet.

very close to 1, emphasizing that the spatial structures are very well captured by the glider fleets. The vertical structure of the PC coefficient is quite homogeneous, taking values larger than 0.9, except in a depth range between 400 and 700 m. There, the PC coefficient presents a peak with weaker values ranging from 0.7 to 0.85. At greater depth, it recovers to values larger than 0.8. Around 400 m, the intensity of the front and of the mesoscale eddies decreases, enabling submesoscale structures as filaments to be more prominent. This effect is illustrated in the left panel of Fig. 11, representing the temperature anomaly field of the control simulation for the model level depths greater than 300 m, normalized by the spatial temperature variance at the corresponding depths. At 330-m depth, the apparent structures are the front and the mesoscale eddies, whereas at 430 m and even more at 550 m, filaments emerge very clearly. From 700 m, filaments are less visible. In the right panel of Fig. 11, where the corresponding fields of the glider data analysis for a 30-glider fleet are plotted, the filament structures are completely missing, giving a slightly deformed picture of the original field. This shortcoming can be completely attributed to the methodology, focusing on mesoscale reconstruction.

From 5 to 10 gliders, the PC coefficient still underlines a good correlation until 400-m depth, with values higher than 0.8. Below this depth, the shortcoming described above is amplified. When the fleet is only constituted of two gliders, the analysis field gives only a bipolar structure, unable to stick to the control field.

3) OBJECTIVE ANALYSIS ERROR

The objective analysis produces the estimate that has the minimum error variance. Along with the analysis field estimated from the glider dataset, it provides also an analysis error field, which can be related to the glider data coverage of the sampled domain. The objective estimate will have a small error when there are sufficient glider data points close in space and time.

The right panel of Fig. 10 represents the percentage of the surface covered by points with an analysis variance error less than 5% of the total variance. With a fleet of 30 gliders, about 99% of the domain is well covered in space and time. From more than 10 gliders, the coverage encompasses 95% of the domain. With two gliders, it falls to only 20% of the domain, highlighting the insufficient spatial and time coverage. It forces the objective analysis to create some structures in the observations' holes, not matching the real field, as it can be seen in the shaded areas of Figs. 7 and 8. Globally, the spatiotemporal coverage is relatively homogeneous along the vertical, with a few variations in the upper 200 m.

In the central panel of Fig. 10, the vertical structure of the PC coefficient for temperature is plotted, computed

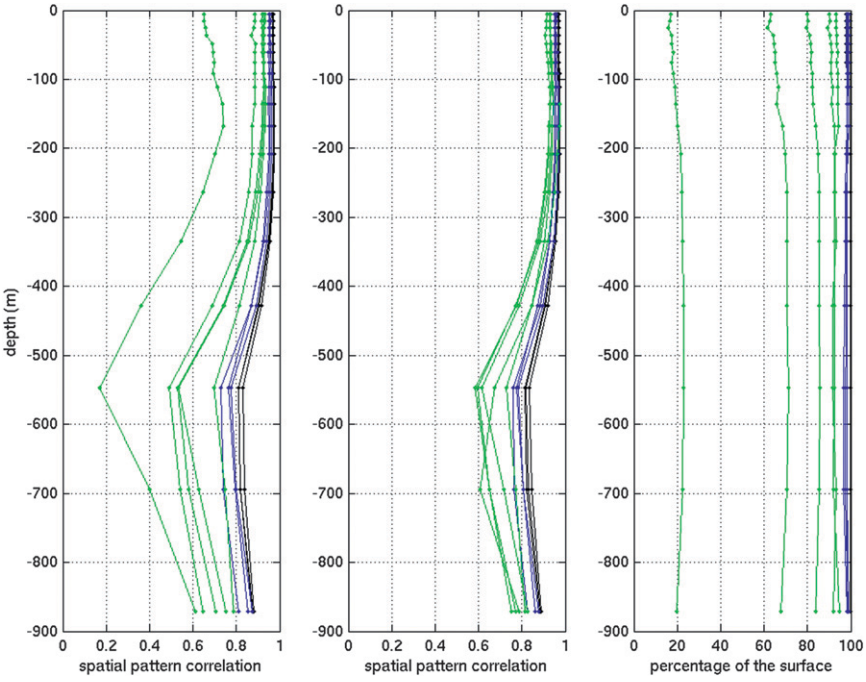

FIG. 10. (left) Vertical structure of T_{PC}. (middle) Vertical structure of T_{PC}, computed with the points whose analysis variance error is less than 5%. (right) Percentage of the surface covered by the points whose analysis variance error is less than 5% of the total variance. In all panels, the curves are plotted in black for 20–30 gliders, in blue for 10–20 gliders, and in green for fewer than 10 gliders, with dots at each vertical model level.

with the points with an analysis error less than 5% of the total variance. Using only the well-covered areas, all the curves stick together with a PC coefficient larger than 0.9 in the surface and subsurface and larger than 0.6 below. It emphasizes that the shortcomings in the reconstructed mesoscale structures are effectively related to a too-weak spatial and time coverage by the gliders. The vertical profiles still exhibit poorer performances around 500 m. The PC anomaly to the mean vertical profile is reduced, but is still apparent. It confirms the hypothesis developed above, that the anomaly present at that depth is not related to a coverage shortcoming but to the chosen method and the spatial scale selection.

5. Discussion

a. Solution of the optimization problem

In this part, we will use the results of the three metrics to determine the optimal solution. As defined before, it corresponds to the minimum number of gliders for which the removal of one glider in the fleet would increase the average normalized errors of the three metrics by more than 1%.

At first, Fig. 9 presents a visual synthesis overview of the objective analysis skill evaluation, as a function of the number of gliders. The results of the three metrics are plotted, averaged on all the grid points of the control model grid, over the four midweek dates. A threshold appears very clearly around 10 gliders. With more than 10 gliders, the error varies slowly, decreasing when the number of gliders is increasing; T_{PC} remains larger than 0.9, highlighting a very good representation of the spatial structures; T_{RMS} is smaller than 1.65 times the target variance of the control simulation; and the glider data coverage is larger than 95%. With fewer than 10 gliders, the error is increasing much faster. Visually, the optimal solution is situated at the slope change.

To determine precisely, for each of the three metrics, the threshold of the slope change corresponding to the optimal solution, we normalize the three metrics to make them comparable. The PC and the objective analysis error metrics are already normalized. With regard to the RMS metric, a few computations are done to enable comparison. Once normalized, the RMS metric is decreasing as the function of the increasing number of gliders. Therefore, the function $(1 - T_{RMS})$ is considered, which is increasing with the number of gliders, like the two other metrics. Because the objective is to determine a threshold for the slope change, it does not have any impact on the results. The three normalized metrics are plotted in the top panel of Fig. 12, as a function of the

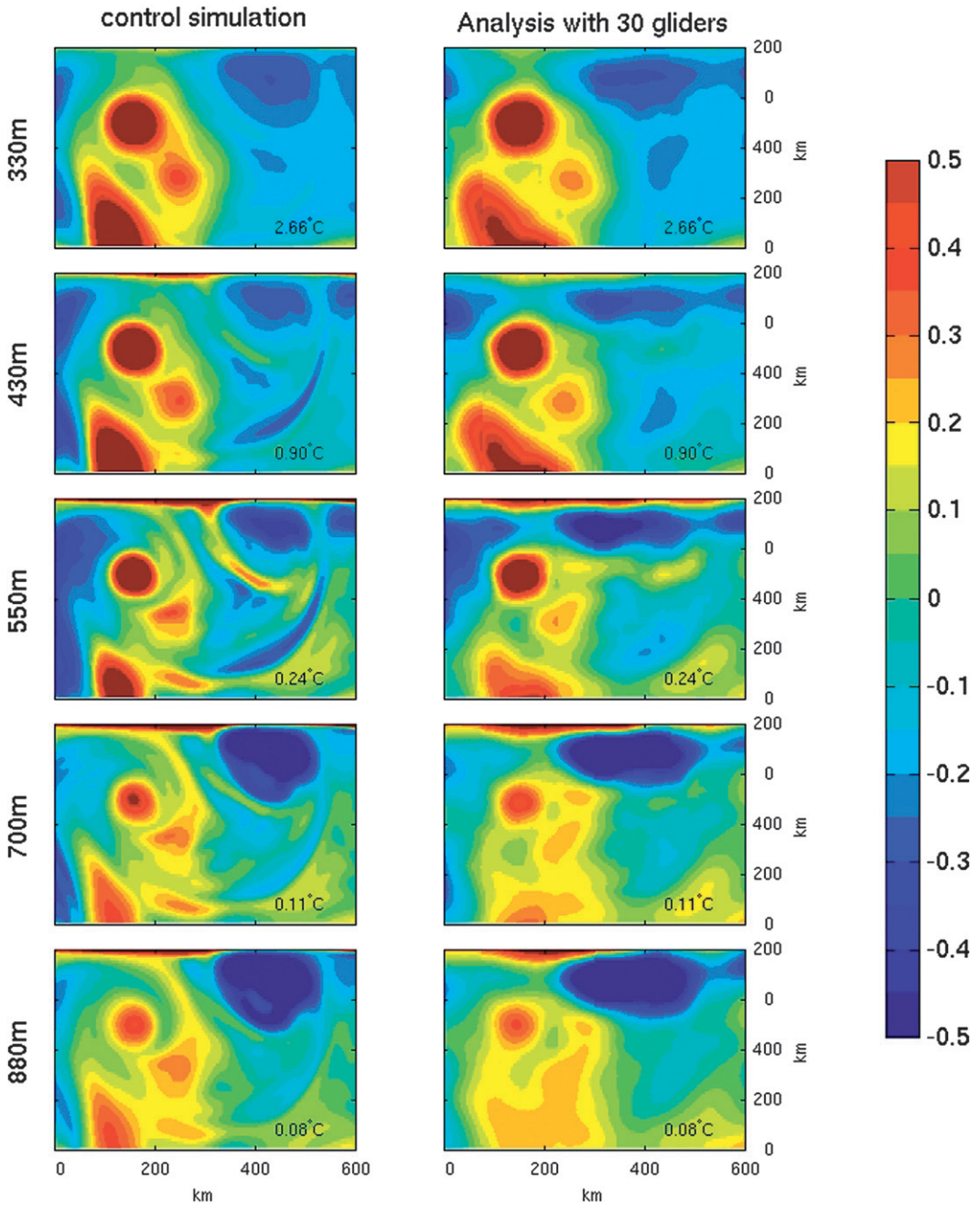

FIG. 11. (left) Horizontal temperature anomaly field of the control simulation for five model levels, normalized by their spatial temperature standard deviation at the corresponding level (value noted in the bottom-right corner). (right) Corresponding fields for the glider data analysis with a 30-glider fleet.

number of gliders. There is clearly a plateau between 10 and 20 gliders. To determine precisely the threshold for the slope change, theoretical functions defined as $y = C_1(1 - C_2/x)$ are fitted to the three normalized metrics (top panel of Fig. 12). They capture well the slopes of the metrics between 6 and 15 gliders. The derivative of the theoretical functions with respect to the number of gliders and their mean are plotted on the bottom panel of Fig. 12. In the figure, the threshold of 1% for the mean derivatives corresponds to 10 gliders. This optimization method based on the three different metrics confirms the previous estimate: in the oceanic configuration of this study, given the goals of the sampling, the optimal solution is a fleet of 10 gliders.

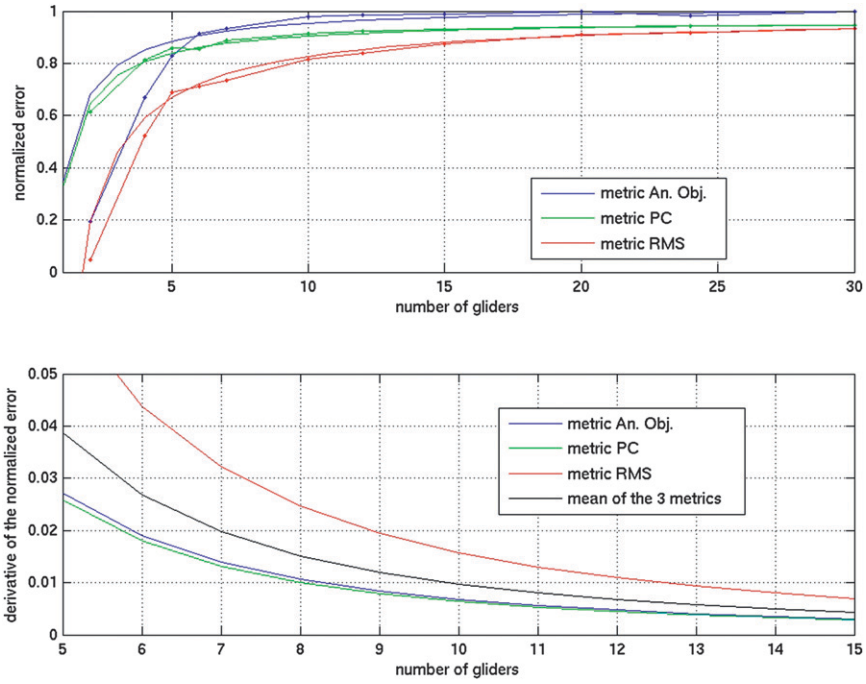

FIG. 12. (top) Normalized error for the three metrics (OA in blue, PC in green, and RMS in red) and theoretical functions fitting to the normalized errors for the three metrics (same colors). (bottom) Derivative of the theoretical functions with respect to the number of gliders (same colors), and mean of the derivatives of the three metrics (black curve).

b. *Guidelines to design an "in situ remote sensing" experiment*

In this study, we have demonstrated that this network configuration with 10 gliders is optimal to obtain a good reconstitution of the original model field, with a multiscale 3D objective analysis, in the particular case of a domain of 600 km × 400 km, on a weekly basis. The errors associated with the analysis of the data in such a configuration have also been quantified. One cannot directly generalize our results to another network presenting a different geometry (unless considering a network that could be decomposed in double comb, which opens some perspectives about complex designs) or in another region with different variability. However, it is worth noting that our results are linked with the spatial and temporal variability scales of the sampled area.

First, the sensitivity study has been based on the gliders' density along the domain length. With a domain length of 600 km, the optimum number of gliders is 10, giving a glider per 60 km, which corresponds to the order of magnitude of the internal deformation radius of Rossby in this region. This plausible relationship can be generalized to other oceanic regions, giving the following assumption: the optimum sampling is obtained with a density of only one glider per deformation radius along the domain length in this double-comb configuration.

Then, the time scale of a week, typical of the evolution of mesoscale structures in this region (Fig. 6), certainly constrains the width of the domain to sample, parallel to the glider trajectories (here, 400 km). We chose it close to twice the mean distance traveled by the gliders during the time scale of a week in our experiment, half of the gliders crossing half of the domain width in one direction and the other half of the fleet crossing the other half of the domain width in the opposite direction. We anticipate that domains characterized by a smaller width would certainly lead to even better estimates of the mesoscale field.

Finally, in this study, the gliders were flying at the speed of 40 cm s^{-1}, relative to water, to enable the gliders to cross the strong Gulf Stream currents (Nevala 2005). The glider speed relative to the water U_g, can be, but marginally, adapted. It can typically vary between 20 and 40 cm s^{-1}, and the impact of a slower glider speed on the gliders' trajectories and on the mean domain crossing speed of the gliders has been tested in a sensitivity experiment. This velocity corresponds to the mean time taken by the gliders to cross the domain, divided by the domain width, independent of the effective length of the gliders' trajectory. It depends on the glider speed relative

to the water and on the statistics (mean, standard deviation, maximum) of the ocean current in the experiment. On the one hand, in the particular oceanic current environment of this study, a threshold of $25\,\mathrm{cm\,s^{-1}}$ has been determined, corresponding to the minimum glider speed necessary for all the gliders to achieve at least one crossing of the domain during the experiment duration. On the other hand, the impact of the glider speed decrease on the glider trajectory has been evaluated. The latter is more deviated when the glider is flowing slower. But it does not affect significantly the spatial coverage quality. However, the mean domain crossing speed of the gliders is linearly related to the glider speed relative to the water, with an estimated coefficient equal to half of the maximum currents' velocity in the particular oceanic current environment of this study. Consequently, given the time scale at which the signal has to be reconstituted and the characteristics of the ocean currents in the region, the domain width has to be adapted to the glider speed.

This gives us guidelines to make an attempt to generalize our results to other configurations. Consider that the internal deformation radius of Rossby R_D and the characteristics of the currents' velocity U_{oc} of the region, the glider speed relative to the water U_g, and the typical time scale of the mesoscale features present in this region at which the signal has to be reconstituted, t, are given. In light of our results, an optimum number of gliders to deploy, N_g, as well as a size of the spatial domain to sample, defined by a domain width l (parallel to the gliders' trajectories) and a domain length L for the perpendicular direction, can be suggested.

Considering the glider network topology used in this experiment, the gliders would have to travel the domain half-width in about a period:

$$t{:}\,\frac{l}{2} = U_c t, \tag{13}$$

with U_c being the mean domain crossing speed of the gliders. In our sensitivity experiment, U_c and U_g are linearly related:

$$U_c = kU_g, \tag{14}$$

with $k = \max(U_{\mathrm{oc}})/2$ for oceanic currents with the following characteristics: a maximum velocity of $1.3\,\mathrm{m\,s^{-1}}$, a mean velocity of $0.3\,\mathrm{m\,s^{-1}}$, and a standard deviation of $0.2\,\mathrm{m\,s^{-1}}$ in the 100 surface meters. Merging Eqs. (13) and (14) gives for the domain width

$$l = 2kU_g t, \tag{15}$$

and the optimum sampling along the domain length L is of one glider per internal deformation radius of Rossby:

$$L = N_g R_D. \tag{16}$$

However, to generalize to other oceanic currents' characteristics, some sensitivity experiments have to be performed to validate the proposed relationship between k and the statistical characteristics of the oceanic current U_{oc}.

A relationship between the survey error and the variability scales of the domain has already been addressed in an idealized study performed by Willcox et al. (2001). In this study, they have developed survey performance metrics that quantify vehicle energy consumption and both spatial undersampling and temporal survey errors. They aim to minimize these errors, by varying the total duration of the survey and its spatial resolution. Some sensitivity experiments show that the minimum error is also strongly tied to the size of the survey domain and to the number of vehicles used. A smaller error will be achieved in the smaller survey domain, and using multiple vehicles was found to be the most beneficial and straightforward method to improve survey performance. It is interesting to test our results using this survey analysis tool. In our study, the survey duration is the same for each experiment, so the temporal survey error does not vary. Besides, the gliders' energy consumption is not a limiting factor. We use a fixed survey domain, and we perform a sensitivity experiment on the number of gliders in the fleet, equivalent to varying the spatial resolution. The combined spatiotemporal survey error can be computed with Eq. (32) in Willcox et al. (2001), using the estimate of the mean spatial resolution, for each fleet of gliders, but the same survey duration. The combined spatiotemporal survey error ranges from 0.35 for 30 gliders to 0.68 for 2 gliders. With 10 gliders, the survey error is 0.45. Using this survey error metric, the choice of 10 gliders as an optimal solution is less obvious than in our statistical analysis. But Willcox et al.'s (2001) survey error metric does not take into account the objective analysis reconstruction method impact, which improves significantly the analysis field, from 10 gliders.

6. Conclusions

This study provides a methodology to assess the capacity of an observing system composed with gliders. By carrying out OSSEs in a midlatitude area in a very high-resolution ocean model (<2 km of horizontal resolution), we have demonstrated the efficiency of a glider fleet to sample a well-defined area at mesoscale in a particular configuration. A network design has been elaborated, in the shape of a ''double comb,'' and the sampling of fleets of 2–30 gliders has been simulated in a control simulation.

With the glider sampled data, a method using objective analysis has been developed to reconstitute the three-dimensional tracer fields at a weekly time scale and at a spatial resolution of 2 km × 2 km. The analysis fields have been compared to the original fields of the control simulation, standing here for the real ocean. Analysis skill evaluation has been performed with three performance metrics: RMS and PC statistical metrics, and a metric based on the objective analysis error. Finally, the optimum number of gliders necessary to obtain a good reconstitution of the original model field has been evaluated. In this particular situation, the optimum number of gliders has been demonstrated to take the value of 10 gliders.

A relationship between the spatial scales of the sampled area, the physical characteristics of the studied region, the chosen time scale, and the optimum number of gliders becomes apparent in our particular experiment. This suggests our results could be generalized to any glider fleet deployment aimed to study the spatiotemporal variability of the mesoscale structures in a given region. A simple model has been proposed, based on this relationship, and could be used to provide a first guess for the design of a glider fleet network. However, sensitivity studies have yet to be done to test the reliability of this simple model in other configurations.

In this study, a method based on objective analysis was used to reconstitute quasi-synoptic images of the ocean at different depths. The shortcomings in the reconstruction are most often related to the coverage, apart from the particular case at 500-m depth, where they are related to the analysis method and more particularly to the spatial scale selection. Therefore, the analysis method provides some depth in understanding of the results, also relevant to design. Moreover, other methods could be used to take into account the information that could be extracted from different datasets (satellite, in situ), using the ocean dynamics, like the data assimilation method. However, the advantage of this objective analysis method is that it is relatively easy to implement. There is no need for a complex numerical model like for the data assimilation method.

This method enabled producing synoptic snapshots of the 1000-m surface layer of the ocean at a given time scale. In the same way as for the temperature, all the other tracer fields that can be measured by gliders, such as salinity, oxygen, fluorescence, or turbidity, could be reconstituted. It could be very useful for designing an observing system aimed at studying the processes involved in the physical–biogeochemical coupling. However, this would require further studies, beyond the scope of this paper, since the variability of these parameters is likely to be slightly different from the temperature field that was studied here.

Operational oceanography becomes widespread. Therefore, the development of a systematic monitoring of the 1000-m surface layer of an oceanic region with a glider network is now achievable and could be a very interesting experiment. It could enable monitoring of the mesoscale structures and their temporal evolution at a given time scale, following the methodology developed in this study, and revisiting the pioneering studies of the MODE experiment (Robinson and Leslie 1985).

In perspective, one could go further in the optimization of the number of gliders to deploy. The first idea would be to study how to combine gliders with other in situ platforms (Argo profiling floats, moorings, ships), in the spirit of Alvarez et al. (2007). Moreover, one could try to optimize the waypoints aimed by the gliders to maintain an optimal network pattern, using a control strategy following the example of Leonard et al. (2010). Some efforts have been made in this study in this direction by considering a piloting algorithm, the heading ''Lekien correction'' (Lekien et al. 2008), enabling the gliders to operate in a region characterized by strong currents. The next step would be to perform adaptive sampling with some gliders, devoted to targeted observations of mesoscale features, revealed by a fixed network, following the approach presented by Lekien et al. (2008) and to carry out an evaluation of the impact of these specific gliders' sampling on the network scores and the gain for the mesoscale (or even submesoscale) structures' reconstitution.

Acknowledgments. We thank the three anonymous reviewers for their constructive scientific remarks, which helped to improve the paper. We thank also Marina Lévy and K. Takahashi for providing us the 1/54° horizontal-resolution simulation of an idealized double gyre, performed in the frame of the GYRE experiment. Finally, a special thanks to Claude Estournel for her responsiveness and availability at the time of the manuscript revision.

APPENDIX

The Heading Correction Methods

The first method is the one implemented in the software on board the real Slocum glider (Webb et al. 2001), named ''current correction.'' At each surfacing, the ocean current is estimated as described in section 2, and used on the subsequent dive to deviate the glider heading. Figure A1 illustrates the different heading corrections' capabilities. The computation of the corrected heading is made at the surfacing time $t = 1$. The waypoint aimed is translated by the ocean current direction $\mathbf{u}$ of the distance corresponding to the estimated distance traveled

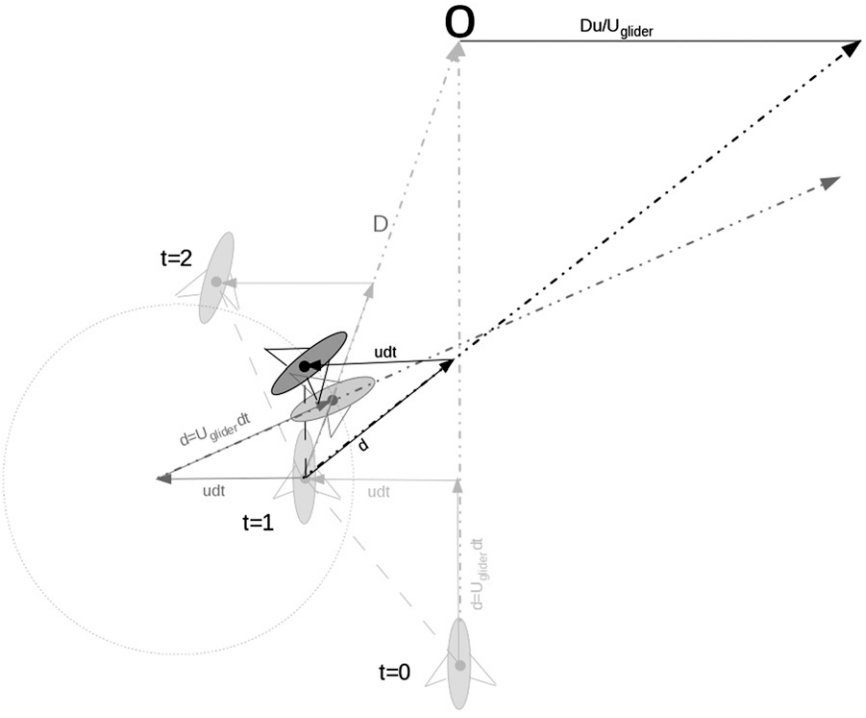

FIG. A1. Successive positions of the glider at the time of surfacing ($t = 0, 1$ and 2) when flying freely to the waypoint (light gray), with the current correction at $t = 2$ (black) and with the Lekien correction at $t = 2$ (dark gray). Ocean current **u** is taken constant in time/space for simplicity.

by the glider carried by the ocean current **u** during the time D/U_{glider} needed to join the waypoint. Following this corrected course (dotted–dashed black arrow), the next surfacing position of the glider is estimated (black glider scheme), adding the fixed distance traveled by the glider $d = U_{\text{glider}}\, dt$ in the corrected heading direction and the ocean current drift deviation **u** dt. In the case represented here, the glider is less deviated than in the ''free flying'' mode but it does not succeed in maintaining the right heading.

In the second method, developed by Lekien et al. (2008), the heading is adjusted to counteract completely the deviation induced by the flow, when it is possible. Two possible cases likely to occur with this method are represented in Fig. A2. In the first case (gray scheme in Fig. A2 or example in Fig. A1), the heading shift counteracts entirely the ocean current deviation and induces a movement in the desired direction. As shown in Fig. A1, the position of the glider at the time $t = 1$ is translated as **u** dt parallel to the ocean current vector **u**. Then, given a radius circle equal to the glider traveled distance $d = U_{\text{glider}}\, dt$, the intersection between this radius circle and the free-flying heading (dotted–dashed light gray arrow) gives the next surfacing position of the glider (dark gray glider scheme).

The heading shift β for full current compensation is given by

$$\sin(\beta) = \mathbf{uGW}/(d|\mathbf{GW}|), \tag{A1}$$

where **u** is the ocean current vector, **GW** is the vector linking the glider position to the waypoint, and d is the traveled distance of the glider between two surfacings. This situation occurs when the right-hand side of the Eq. (A1) is smaller than 1. In the other cases (black scheme in Fig. A2), the currents cannot be compensated completely, and another heading shift β is computed, as the angle that minimizes heading deviation:

$$\beta = p/2 + tg^{-1}(d/|\mathbf{u}|) + \sin^{-1}(\mathbf{u}\times\mathbf{GW})/(|\mathbf{u}||\mathbf{GW}|). \tag{A2}$$

In the first case, as illustrated in Fig. A1, this method sticks at each surfacing the glider trajectory to the direct trajectory. In both cases, it is very efficient at preventing the glider from deviating too much. In the simulations carried out in this study, the Lekien correction has been enabled, and it significantly improved the glider fleet trajectory, although especially strong fronts and eddies currents are crossed. This is the closer method to the one recommended by Davis et al. (2009, p. 186), who provide

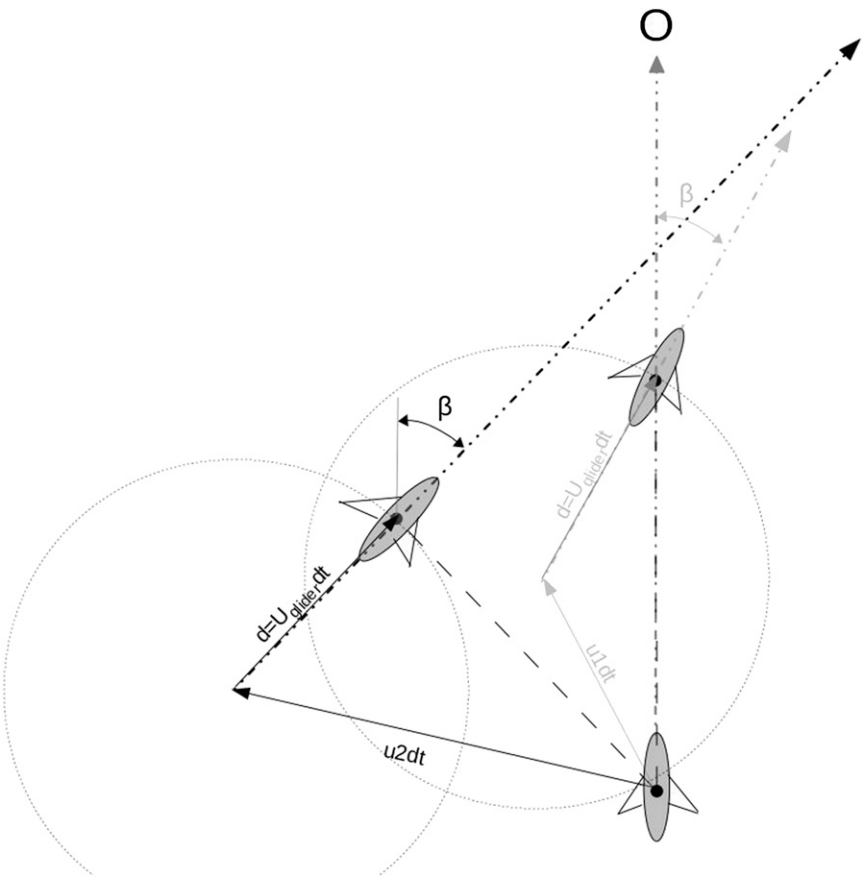

FIG. A2. Positions of the glider at the time of surfacing with the Lekien correction, in the two possible cases. With the ocean current $\mathbf{u}_1$, the heading shift counteracts entirely the current deviation (light gray scheme). When deviated by the ocean current $\mathbf{u}_2$, the heading deviation is only minimized (black scheme).

the following steering rule: ''the vehicle heads directly to the destination when good progress is possible and heads across the current when progress is slow.''

REFERENCES

Alvarez, A., B. Garau, and A. Caiti, 2007: Combining networks of drifting profiling floats and gliders for adaptive sampling of the ocean. *Extended Abstracts, 2007 IEEE Int. Conf. on Robotics and Automation,* Rome, Italy, IEEE, 157–162.

Berezutskii, A. V., S. E. Maximov, V. E. Sklyarov, and R. L. Gordon, 1991: Deep ADCP velocity measurements in the Gulf Stream. *J. Atmos. Oceanic Technol.,* **8,** 884–887.

Böhme, L., and U. Send, 2005: Objective analysis of hydrographic data for referencing profiling float salinities in highly variable environments. *Deep-Sea Res. II,* **52,** 651–664.

Bouffard, J., A. Pascual, S. Ruiz, Y. Faugère, and J. Tintoré, 2010: Coastal and mesoscale dynamics characterization using altimetry and gliders: A case study in the Balearic Sea. *J. Geophys. Res.,* **115,** C10029, doi:10.1029/2009JC006087.

Castelao, R., S. Glenn, O. Schofield, R. Chant, J. Wilkin, and J. Kohut, 2008: Seasonal evolution of hydrographic fields in the central Middle Atlantic Bight from glider observations. *Geophys. Res. Lett.,* **35,** L03617, doi:10.1029/2007GL032335.

Cheney, R. E., and J. G. Marsh, 1981: Seasat altimeter observations of dynamic topography in the Gulf Stream region. *J. Geophys. Res.,* **86** (C1), 473–483.

Davis, R. E., N. E. Leonard, and D. M. Fratantoni, 2009: Routing strategies for underwater gliders. *Deep-Sea Res. II,* **56,** 173–187.

Dobricic, S., N. Pinardi, P. Testor, and U. Send, 2010: Impact of data assimilation of glider observations in the Ionian Sea (eastern Mediterranean). *Dyn. Atmos. Oceans,* **50,** 78–92.

Garau, B., A. Alvarez, and G. Oliver, 2005: Path planning of autonomous underwater vehicles in current fields with complex spatial variability: An A* approach. *Proc. IEEE Int. Conf. on Robotics and Automation,* Barcelona, Spain, IEEE, 194–198.

——, ——, and ——, 2006: AUV navigation through turbulent environments supported by onboard H-ADCP. *Proc. IEEE Int. Conf. on Robotics and Automation,* Orlando, FL, IEEE, 3556–3561.

Graver, J. G., R. Bachmayer, N. E. Leonard, and D. M. Fratantoni, 2003: Underwater glider model parameter identification. *Proc. 13th Int. Symp. on Unmanned Untethered Submersible Technology,* Durham, NH, Office of Naval Research, 12 pp.

Griffiths, R. W., and E. J. Hopfinger, 1984: The structure of mesoscale turbulence and horizontal spreading at ocean fronts. *Deep-Sea Res.,* **31A,** 245–269.

Hazeleger, W., and S. S. Drijfhout, 1998: Mode water variability in a model of the subtropical gyre: Response to anomalous forcing. *J. Phys. Oceanogr.,* **28,** 266–288.

Hodges, B. A., and D. M. Fratantoni, 2009: A thin layer of phytoplankton observed in the Philippine Sea with a synthetic moored array of autonomous gliders. *J. Geophys. Res.,* **114,** C10020, doi:10.1029/2009JC005317.

Lekien, F., L. Mortier, and P. Testor, 2008: Glider coordinated control and Lagrangian coherent structures. *Second IFAC Workshop Navigation, Guidance and Control of Underwater Vehicles,* Killaloe, Ireland, International Federation of Automatic Control, 125–130, doi:10.3182/20080408-3-IE-4914.00023.

Leonard, N. H., D. A. Paley, F. Lekien, R. Sepulchre, D. M. Fratantoni, and R. E. Davis, 2007: Collective motion, sensor networks, and ocean sampling. *Proc. IEEE,* **95,** 48–74, doi:10.1109/JPROC.2006.887295.

——, ——, R. E. Davis, D. M. Fratantoni, F. Lekien, and F. Zhang, 2010: Coordinated control of an underwater glider fleet in an adaptive ocean sampling field experiment in Monterey Bay. *J. Field Rob.,* **27,** 718–740.

Lévy, M., D. Iovino, S. Masson, G. Madec, P. Klein, A.-M. Tréguier, and K. Takahashi, 2009: Remote impacts of submesoscale dynamics on new production. *Mercator Ocean Quaterly Newsletter,* No. 35, Mercator Ocean, Ramonville Saint-Agne, France, 13–19.

——, P. Klein, A.-M. Tréguier, D. Iovino, G. Madec, S. Masson, and K. Takahashi, 2010: Modifications of gyre circulation by sub-mesoscale physics. *Ocean Modell.,* **34,** 1–15, doi:10.1016/j.ocemod.2010.04.001.

——, D. Iovino, L. Resplandy, P. Klein, G. Madec, A.-M. Tréguier, S. Masson, and K. Takahashi, 2012: Large-scale impacts of submesoscale dynamics on phytoplankton: Local and remote effects. *Ocean Modell.,* **43–44,** 77–93.

L'Hévéder B., J.-M. Lellouche, P. Lherminier, L. Mortier, T. Terre, P. Testor, and G. Vinay, 2009: Operational forecast of glider trajectories during EGO 2008 operations in the Mediterranean Sea using Mercator Ocean forecast. *Mercator Ocean Quarterly Newsletter,* No. 32, Mercator Ocean, Ramonville Saint-Agne, France, 33–38.

Madec G., 2008: NEMO ocean engine. Version 3, IPSL Note du Pôle de Modélisation 27, 209 pp.

Mann, K., and J. Lazier, 2005: *Dynamics of Marine Ecosystems: Biological–Physical Interactions in the Oceans*. 3rd ed. John Wiley & Sons, 512 pp.

Nevala, A. E., 2005: A glide across the Gulf Stream: Remote-controlled Spray's historic step heralds new era of ocean exploration. *Oceanus,* **44,** 10. [Available online at http://www.whoi.edu/oceanus/index.do.]

Oke, P. R., P. Sakov, and E. Schulz, 2009: A comparison of shelf observation platforms for assimilation in an eddy-resolving ocean model. *Dyn. Atmos. Oceans,* **48,** 121–142.

Olbers, D., 1978: The Mid-Ocean Dynamics Experiment. *Deep-Sea Res.,* **25,** 859–910.

Onken, R., A. Alvarez, V. Fernandez, G. Vizoso, G. Basterretxea, J. Tintoré, P. Haley, and E. Nacini, 2007: A forecast experiment in the Balearic Sea. *J. Mar. Syst.,* **71,** 79–98.

Pietri, A., P. Testor, V. Echevin, A. Chaigneau, L. Mortier, G. Eldin, and C. Grados, 2013: Finescale vertical structure of the upwelling system off southern Peru as observed from glider data. *J. Phys. Oceanogr.,* **43,** 631–646.

Ramp, S. R., and Coauthors, 2009: Preparing to predict: The Second Autonomous Ocean Sampling Network (AOSN-II) Experiment in the Monterey Bay. *Deep-Sea Res. II,* **56,** 68–86.

Robinson, A. R., and W. G. Leslie, 1985: Estimation and prediction of oceanic eddy fields. *Prog. Oceanogr.,* **14,** 485–510.

Roemmich, D., 1983: Optimal estimation of hydrographic station data and derived fields. *J. Phys. Oceanogr.,* **13,** 1544–1549.

——, and Coauthors, 2009: The Argo program: Observing the global ocean with profiling floats. *Oceanography,* **22** (2), 34–43.

Rudnick, D. L., R. E. Davis, C. C. Eriksen, D. M. Fratantoni, and M. J. Perry, 2004: Underwater gliders for ocean research. *Mar. Technol. Soc. J.,* **38** (2), 73–84.

Siegel, A., J. B. Weiss, J. Toomre, J. C. McWilliams, P. S. Berloff, and I. Yavneh, 2001: Eddies and vortices in ocean basin dynamics. *Geophys. Res. Lett.,* **28,** 3183–3186.

Stammer, D., 1997: Global characteristics of ocean variability estimated from regional TOPEX/POSEIDON altimeter measurements. *J. Phys. Oceanogr.,* **27,** 1743–1769.

——, 1998: On eddy characteristics, eddy transports, and mean flow properties. *J. Phys. Oceanogr.,* **28,** 727–739.

Stommel, H., 1989: The Slocum mission. *Oceanography,* **2** (1), 22–25.

Testor, P., and Coauthors, 2007: European gliding observatories EGO. *Coriolis Newsletter,* No. 4, IFREMER, Plouzané, France, 11–12.

——, and Coauthors, 2010: Gliders as a component of future observing systems. *Proceedings of the OceanObs'09: Sustained Ocean Observations and Information for Society.* Vol. 2, ESA Publ. WPP-306, doi:10.5270/OceanObs09.cwp.89.

Webb, D. C., P. J. Simonetti, and C. P. Jones, 2001: Slocum: An underwater glider propelled by environmental energy. *IEEE J. Oceanic Eng.,* **26,** 447–452.

Willcox, J. S., J. G. Bellingham, Y. Zhang, and A. B. Baggeroer, 2001: Performance metrics for oceanographic surveys with autonomous underwater vehicles. *IEEE J. Oceanic Eng.,* **26,** 711–725.

Zhang, Y., J. G. Bellingham, and Y. Chao, 2010: Error analysis and sampling strategy design for using fixed or mobile platforms to estimate ocean flux. *J. Atmos. Oceanic Technol.,* **27,** 481–506.